Influence of Magnetic Clouds on Variations of Cosmic Rays in November 2004

Xiao Xia Yu · Hong Lu · Gui Ming Le · Feng Shi

Abstract We investigate the effects of two magnetic clouds on hourly cosmic-ray intensity profiles in the Forbush decrease events in November 2004 observed by 47 ground-based neutron-monitor stations. By using a wavelet decomposition, the start time of the main phase in a Forbush decrease event can be defined, and then clearer definitions of initial phase, main phase, and recovery phase are proposed. Our analyses suggest that the main phase of this Fd event precedes the arrival time of the first magnetic cloud by about three hours, and the Fds observed at the majority (39/47) of the stations were found to originate from the sheath region as indicated by large fluctuations in magnetic field vectors at 19:00 UT on 7 November 2004, regardless of the station location. In addition, about 45% of the onset times of the recovery phase in the Forbush decreases took place at 04:00 UT on 10 November, independent of the station position. The results presented here support the hypothesis that the sheath region between the shock and the magnetic cloud, especially the enhanced turbulent magnetic field, results in the scattering of cosmic-ray particles, and causes the following Forbush decreases. Analysis of variation profiles from different neutron monitors reveals the global simultaneity of this Forbush decrease event. Moreover, we infer that the interplanetary disturbance was asymmetric when it reached the Earth, inclined to the southern hemisphere. These results provide several observational constraints for more detailed simulations of the Forbush decrease events with time-dependent cosmic-ray modulation models.

X.X. Yu (✉) · H. Lu · F. Shi
Key Laboratory of Particle Astrophysics, Institute of High Energy Physics, Chinese Academy of Sciences, Beijing 100049, China
e-mail: xxyu@ihep.ac.cn

G.M. Le
National Center for Space Weather, China Meteorological Administration, Beijing 100081, China

1. Introduction

There are abundant observational evidences suggesting that a good fraction of intense solar-terrestrial events involves a wide series of activities, including solar flares, CMEs, shocks, ICMEs/MCs, geomagnetic storms, and Forbush decreases simultaneously. Coronal mass ejections (CMEs) occurring close to the solar disk center are large-scale and transient structures which are expelled from the Sun and travel toward the external heliosphere, influencing the geomagnetic field when their magnetic configurations are appropriate (Gopalswamy *et al.*, 2001; Gopalswamy, Yashiro, and Akiyama, 2007). Counterparts to CMEs observed by satellites at 1 AU are defined as interplanetary coronal mass ejections (ICMEs). A subclass of ICMEs, called magnetic clouds (MCs), carrying a large amount of magnetic flux and helicity, is contrasted to the ICMEs in some published literature (Qiu *et al.*, 2007; Gopalswamy *et al.*, 2008; Nakwacki *et al.*, 2008). From an observational point of view, magnetic clouds are generally characterized by the change in the magnetic field direction almost monotonically from south (north) to north (south), more enhanced magnetic field than in the vicinity (strength greater than 10 nT) (Cane and Richardson, 1995), and a depressed proton temperature with a low plasma beta value (β) (Burlaga *et al.*, 1981; Zhang and Burlaga, 1988). Theoretical studies on the field configuration of magnetic clouds may reveal the process of formation and propagation of single or multiple clouds and furthermore determine the orientation of the axis of the cloud (Wang *et al.*, 2005; Dasso *et al.*, 2006).

Accompanied by the above-mentioned interplanetary events, on the one hand, geomagnetic storms due to long-lasting interplanetary convection electric fields are observed at low- and mid-latitude stations as a sharp reduction in the horizontal component of the geomagnetic field (Gonzalez *et al.*, 1994). Secondly, a short-term depression in the count rates of galactic cosmic rays (GCRs, high energy protons transported through the interplanetary medium and entering the terrestrial atmosphere) is recorded by ground-based neutron-monitor stations. This event, called the Forbush decrease (Fd), could give us new insight into the nonperiodic modulation of cosmic rays stemming from solar activities. Particularly, severe geomagnetic storms along with Forbush decreases in cosmic ray variation have precursor effects that could be applied in forecasting space weather conditions (Dorman, Iucci, and Villoresi, 1995; Belov *et al.*, 2003; see Section 18.12 of Dorman, 2004 for more details; Dorman, 2005; Mavromichalaki *et al.*, 2006). In general, it is thought that CMEs and shocks/sheath associated with them are the underlying causes of geomagnetic storms and Fds (Zhang and Burlaga, 1988; Cane 2000a; Cane, Richardson, and Cyr, 2000b; Kudela and Brenkus, 2004; Badruddin, 2006; Dorotovic *et al.*, 2008). A numerical simulation of Fds has shown that the magnitude of the Fds is sensitive to the amplitude of interplanetary disturbances (Le Roux and Potgieter, 1991). The cause of Fds is an open issue which entails three kinds of long-recognized views, namely

 i) The sweeping effect of the interplanetary shock.
ii) The gradient drift in the shock with well-ordered structure.
iii) Deflection of the incoming cosmic-ray particles owing to an intense interplanetary magnetic field structure exited in the region between a shock front and its driver (Mulder and Moraal, 1986; Cheng, Sarris, and Dodopoulos, 1990; Venkatesan *et al.*, 1992; Ananth and Venkatesan, 1993; Rana, Sharma, and Yadav, 1996; Badruddin, 2002; Su, Yu, and Yong, 2008).

However, no consensus has been reached on which physical process is dominant in producing the transient depression in the galactic cosmic rays (Badruddin 2000, 2002; Su, Yu,

and Yong, 2008). A simultaneous ground-level detection of cosmic rays at different cutoff rigidities could provide information on the energy spectra of GCRs (Eroshenko *et al.*, 2004; Kane, 2006). The database of the world-wide network of neutron-monitor stations collected by IZMIRAN (http://cr0.izmiran.rssi.ru/mosc/main.htm) provides us with complete hourly data of cosmic ray intensity (Mavromichalaki *et al.*, 2006; Belov *et al.*, 2007). However, the hourly data are closely related to the yield function of each detector.

From 1 November to 28 November 2004, transient decreases in cosmic rays due to solar eruptions were recorded by 47 ground-based neutron-monitor stations at the Earth, with a sudden onset, reaching a minimum within several days, followed by a quasi-exponential recovery phase lasting for half a month. So far a lot of work has been carried out in order to disentangle a series of phenomena that took place in NOAA active region (AR) 10 696 from various scales and angles (Culhane *et al.*, 2007; Dasso *et al.*, 2007; Harra *et al.*, 2007; Jamsen *et al.*, 2007; Longcope *et al.*, 2007; Pohjolainen *et al.*, 2007; Qiu *et al.*, 2007; Wang *et al.*, 2007; Alania and Wawrzynczak, 2008; Nakwacki *et al.*, 2008; Usoskin *et al.*, 2008). Longcope *et al.* (2007) constructed a three-dimensional topological magnetic field model of the large two-ribbon flare that occurred at 16:15 UT on 7 November 2004, and gave a hint on the reconnection process to match the magnetic configuration observed. In addition, formation and development of trans-equatorial activities, including trans-equatorial loops, trans-equatorial filaments, and trans-equatorial brightening, were examined by EUV images, X-ray flux profiles, full-disk magnetograms, and Hα images, respectively (Wang *et al.*, 2007). IPS (interplanetary scintillation) observations of CMEs (on 7 November 2004, 16:54 UT) along with the coronagraph images from SOHO/LASCO have revealed uncertainties in the methods of estimating the transit speeds of CMEs (Culhane *et al.*, 2007; Pohjolainen *et al.*, 2007). Comparing the observations from IPS and SMEI (*Solar Mass Ejection Imager*), the speed and density of CMEs based on a 3-D kinematic model were reconstructed (Bisi *et al.*, 2008). To date, quantitative research has been carried out to reveal a one-to-one relationship among CMEs, shocks and ICMEs/magnetic clouds (Tables 1 and 2 in Harra *et al.*, 2007; Tables 1 and 2 in Qiu *et al.*, 2007; Table 6 in Pohjolainen *et al.*, 2007; Figure 9 in Culhane *et al.*, 2007). From 5 to 11 November 2004, two MCs were observed by the ACE and WIND satellites and have been analyzed in detail (Harra *et al.*, 2007; Dasso *et al.*, 2007). Harra *et al.* (2007) suggested that the axes of two magnetic clouds with opposite magnetic orientation lay parallel to or nearly on the ecliptic plane from 7 November to 10 November. With regard to the boundaries of the expanding MC whose existence was confirmed by Dasso *et al.* (2007), Harra *et al.* (2007) and Longcope *et al.* (2007) selected a similar starting time and stop time with Qiu *et al.* (2007). Furthermore, Dasso *et al.* (2007) computed the azimuthal flux and the axial flux in the MC observed by the Wind spacecraft during 9–10 November 2004, and obtained an accurate orientation of the cloud axis. Comparing favorably with results of Qiu *et al.* (2007), Nakwacki *et al.* (2008) proposed the precise orientation of the MC for $\theta = 23°$ and $\phi = 274°$, occurring from 9 to 10 November 2004 (for details of θ and ϕ, see Nakwacki *et al.*, 2008).

On the basis of the study of variations of the ionospheric parameters deduced from ionosondes, terrestrial effects of the above-mentioned solar events have been revealed. A large-scale disturbance was detected along the propagation direction, as well as southwestward velocities of 200 m s^{-1} and 400 m s^{-1} on average on 8 and 10 November 2004, respectively (Yermolaev *et al.*, 2005; Afraimovich *et al.*, 2006; Pirog *et al.*, 2007). Furthermore, injection of electromagnetic energy and kinetic energy into the low ionosphere, and the characteristics of the vertical distribution of electron density in the F2 region during the magnetic storms were presented (Panasenko and Chernogor, 2007; Grigorenko *et al.*, 2007).

In the case of the ground-based neutron-monitor observations in November 2004, recent work has concentrated on several specific cases or statistical studies to reveal the energy dependence of the recovery time in the Fd (Usoskin *et al.*, 2008; Jamsen *et al.*, 2007). But the above-mentioned research seems fragmentary for the interval studied. For example, Alania and Wawrzynczak (2008) found that the exponent of the power law rigidity spectrum had a trend of hardening – softening along with the evolution of the Fd, based on daily data from 22 neutron monitors and the Nagoya muon telescope.

Our present work will focus on the influence of magnetic clouds on the time variation of cosmic rays, particularly on the resulting Fd. Therefore, other aspects and processes related to this event are beyond our scope in this paper. In order to combine spacecraft measurements and ground-based neutron-monitor observations into a coherent scenario on the solar – terrestrial environment, our analysis, which includes the measurement of the magnetic clouds at 1 AU and the data from ground-based neutron monitors, will be presented in Section 2. Section 3 will be dedicated to a clearer definition of the initial phase, main phase, and recovery phase in the Fd event. Statistical studies of sample data deduced from the world-wide network of neutron monitors will also be carried out in detail. Section 4 will be devoted to the discussion of our results and further speculations.

2. Characteristics of Magnetic Clouds and Their Influences on Cosmic Rays

Fast coronal mass ejections (CMEs), X-class flares, interplanetary shocks, ICMEs/magnetic clouds, geomagnetic storms, and significant Forbush decreases were observed during a series of intense solar activities from 3 to 28 November 2004. In total, 24 partial or full halo CMEs during the period from 3 to 7 November 2004, initially traveling at 679 km s^{-1} on average (computed based on http://cdaw.gsfc.nasa.gov/CME_list/UNIVERSAL/2004_11/univ2004_11.html), impacted the Earth causing the two largest geomagnetic storms from 1 October to 31 December 2004 (the minimum D_{st} values were -373 nT at 06:00 UT on 8 November and -289 nT at 09:00 UT on 10 November, respectively). In addition, as the ICMEs crossed the vicinity of the Earth, the upstream measurements of plasma density and magnetic field vector from ACE and Wind spacecraft were obtained, and we will compare them with the above-mentioned data. The interplanetary shocks associated with these CMEs, and the arrival times and speeds of the associated magnetic clouds at the Earth were estimated and published in previous studies (Dasso *et al.*, 2007; Harra *et al.*, 2007; Longcope *et al.*, 2007).

Variations of primary solar-wind parameters obtained with Wind and ACE spacecraft are compared with the data of cosmic rays from 7 to 13 November 2004 in Figures 1 and 2. Before the magnetic clouds arrived at the Earth, the strength of the magnetic field (B), proton temperature (T_p), and proton density (N_p) were enhanced due to the preceding shocks. However, a stronger magnetic field (B) and a depressed proton temperature (T_p) with a low plasma beta ($\beta < 0.1$) were observed inside the magnetic cloud. It is obvious that the long duration of the large southward component of IMF (B_z) is in good agreement with the observed sharp decrease in the D_{st} index. In other words, B_z is the dominating factor in causing the geomagnetic storms observed from 1 October to 31 December 2004. Because of the expansion inside the MC, the peak of the magnetic field strength would shift to the leading edge of the cloud. In addition, five episodes of sudden commencement of geomagnetic storms, each of which could be considered as the geomagnetic signature of the shock arrival, were found to match five out of six shocks which were identified by Harra *et al.* (2007), except for shock five (at 18:20 UT on 9 November).
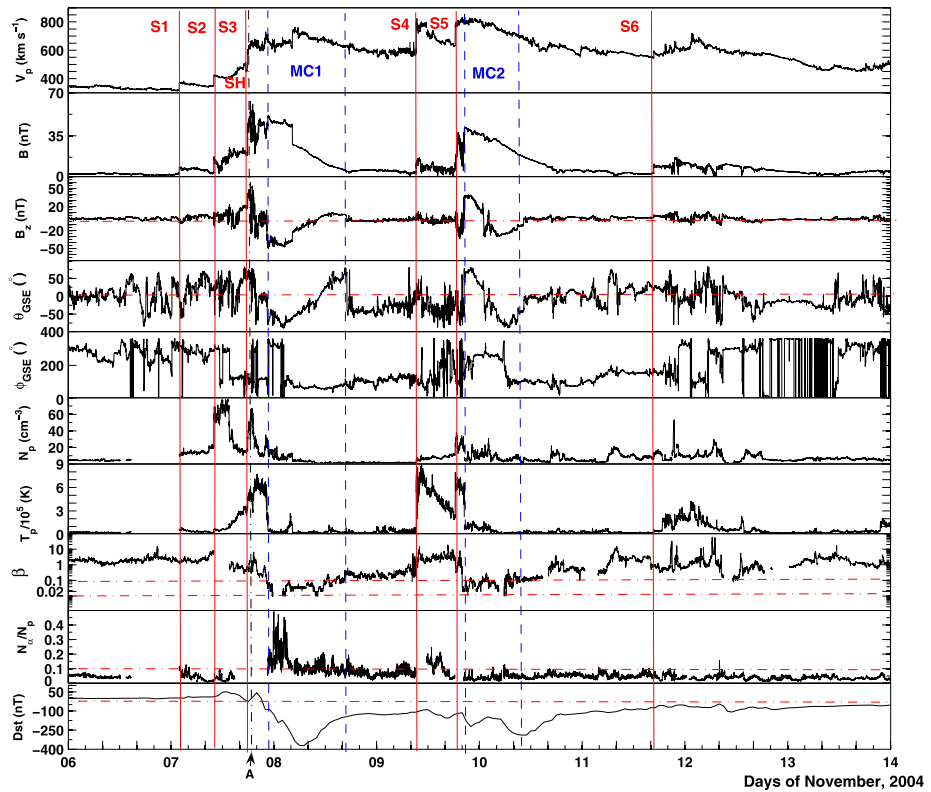
Figure 1 Time variations of parameters characterizing the solar wind and interplanetary medium observed by ACE and Wind from 6 to 13 November 2004. From top to bottom: the solar-wind plasma speed (V_p), the magnetic field strength (B), the southward component of IMF (B_z), latitude (θ_{GSE}) and longitude (ϕ_{GSE}) angles of B in the Geocentric Solar Ecliptic (GSE) coordinates, solar-wind plasma proton density (N_p), solar-wind plasma temperature (T_p), plasma beta (β), number density ratio of alpha to proton (N_α/N_p), and D_{st} index, respectively. SH stands for the sheath region. Six red vertical lines, labeled SH1–SH6, mark the arrival time of the interplanetary shock at the Earth, and four blue dash-dot lines indicate the region of two magnetic clouds (MC1 and MC2). A black dash-dot line, marked with black arrow A, signifies the time when the catastrophe point occurs in the CR variation (7 November 2004, 19:00 UT).

The arrival of the shock at the Earth could be identified by an abrupt increase in the solar-wind plasma speed (V_p) (in Figure 1), and the shock was followed by a turbulent sheath as indicated by enhanced fluctuations in the magnetic field vectors. Also, the sheath was followed by a magnetic cloud in which the direction of the magnetic field changed almost monotonically from south (north) to north (south) within one day, respectively. In order to investigate the relation between the magnetic cloud and D_{st} index, we have applied the classification introduced by Zhang and Burlaga (1988) and Marcz (1992) to divide the magnetic clouds into two categories, namely the SN cloud (in which the magnetic field is initially directed southward and is changing northward) and the NS cloud (with a reverse behavior with reference to the magnetic field), respectively. Generally the minimum of D_{st} index corresponding to SN clouds is deeper than for the case of NS clouds, and the recovery time of the D_{st} index to the pre-event level is longer in the case of SN clouds than in the case of NS clouds. The above-mentioned features are in accordance with Marcz's (1992) conclusion. As seen in Figure 1, the onset time of the geomagnetic activity indicated by the
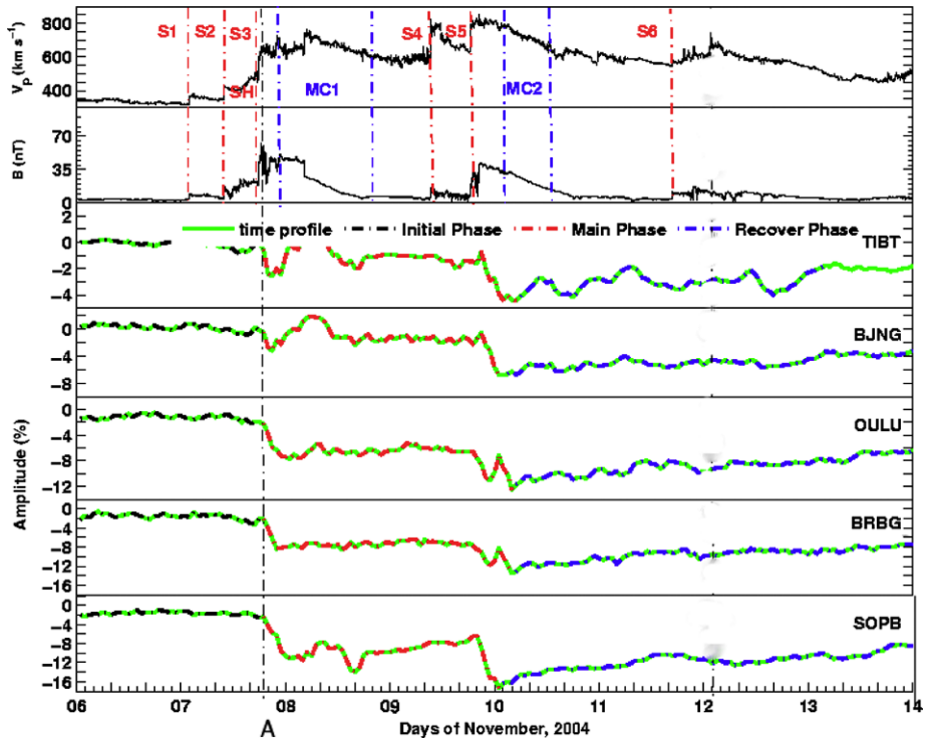
Figure 2 Time profiles of the solar-wind plasma speed (V_p), magnetic field strength (B), and hourly intensity profiles of the TIBT, BJNG, OULU, BRBG and SOPB neutron monitors. SH stands for the sheath region. Six red vertical lines SH1 – SH6, four blue dash-dot lines (MC1 and MC2), and the black dash-dot line have the same meaning as in Figure 1.

decrease in D_{st} index matched the arrival time of the SN cloud, but it lagged behind the launch time of the NS cloud in which the magnetic field was northward at the onset. It is in agreement with the view expressed by Zhang and Burlaga (1988). It is further confirmed that the southward IMF in the sheath and the magnetic cloud is the major source in triggering geomagnetic storms.

Figure 2 shows the time profiles of the solar-wind plasma speed (V_p), magnetic field strength (B), and hourly intensity profiles of the neutron monitors at TIBT, BJNG, OULU, BRBG, and SOPB. Here, we have adopted the hourly neutron-monitor data, namely a temporal resolution different from spacecraft measurements. Different from Ifedili's (2006) research, we could not discriminate a lull region which was located between the sheath and the magnetic cloud on the basis of rms behavior of the IMF components. Typically, two-step Fds were observed in five neutron-monitor stations in Figure 2; the first step was associated with the structure within the shock front and sheath region, and the second step was related to the passage of the MCs, supporting the conclusion drawn by Barnden (1973). In comparison with the difference in geomagnetic storms driven by sheath regions and magnetic clouds shown by Pulkkinen *et al.* (2007), various influences from sheath regions and the passages of magnetic clouds on cosmic rays need further investigation on the basis of the statistical data.

3. Analysis of Ground-Based Neutron-Monitor Observation

3.1. Definition of Three Phases

So far no unified definitions for the initial phase, main phase, and recovery phase in Fds have been established firmly. A representative diagram defining the initial phase, main phase, and recovery phase in a Forbush event is presented in Figure 3. Because the Haar wavelet transform could detect discontinuities in the signal, we first define the onset time of the main phase in a Forbush event as the earliest one of several catastrophe points seen in the wavelet decomposition in the selected time window, equivalent to the end time of the initial phase (T_2 in Figure 3). Then the time of the first intensity maximum before the earliest catastrophe point is selected as the onset time of the initial phase (T_1 in Figure 3), and the time of the minimum intensity serves as the end time of the main phase (T_3 in Figure 3), corresponding to the onset time of the recovery phase. Because of a diurnal modulation in GCR intensity at the Earth with an amplitude of 1% on average, the time when the percentage variation
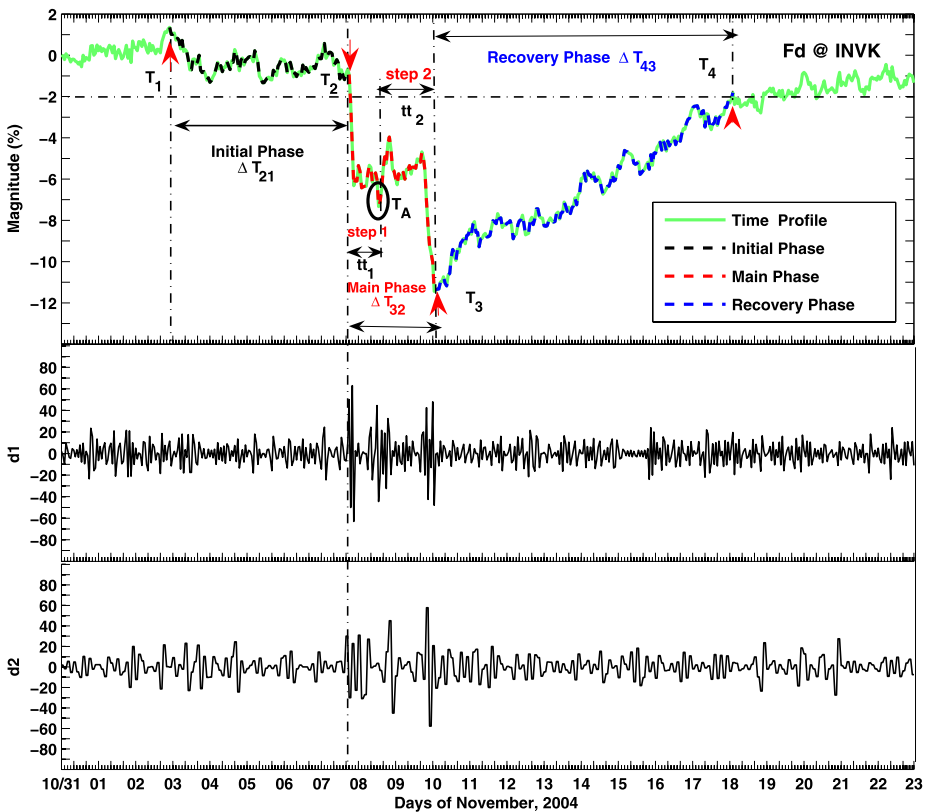
Figure 3 A representative diagram defining the initial phase, main phase, and recovery phase in a Forbush event. From top to bottom are intensity variation of INVK station (upper panel), the first order of the wavelet decomposition coefficient (d1, middle panel) and the second order of the wavelet decomposition coefficient (d2, lower panel). $T_1 - T_4$ indicate the onset time of the initial phase (T_1), the end time of the initial phase (*i.e.* the onset time of the main phase, T_2), the end time of the main phase (*i.e.* the onset time of the recovery phase, T_3) and the end time of the recovery phase (T_4), respectively. ΔT_{21}, ΔT_{32}, and ΔT_{43} state the durations of the initial phase, main phase, and recovery phase, respectively.

reaches -2% is regarded as the end time of the recovery phase in the Fd (T_4 in Figure 3). The above-mentioned definitions on the phases in Forbush events are different from results due to Su, Yu, and Yong (2008), which did not take into account multi-step Forbush decreases.

3.2. Data Analysis

Cosmic ray variations from 47 neutron monitors collected by IZMIRAN have been analyzed together to examine the declines in the count rates. In Figures 4 and 5, we depict the geographic distribution and the longitudinal distribution of the stations. In addition, Table 1 summarizes the obtained results from hourly cosmic ray intensities registered by 47 ground-based neutron monitors for the investigated events with an amplitude $> 4\%$ during the interval studied. The amplitude of Fd listed in Table 1 is calculated as $100 \cdot (N - N_{\mathrm{b}})/N_{\mathrm{b}}$, where N_{b} is the hourly counting rate in the undisturbed period from 7 October to 6 November 2004, selected as the pre-event background in each involved neutron monitor, and N is the hourly count during the maximum decrease of the cosmic ray intensity in each station. Slight differences in the value of N_{b} among the stations will not influence the identifications of the start time and durations of various phases in Forbush events. To fully understand a realistic Forbush event at the Earth, it is necessary to list all the effective observational results from the neutron monitors as in Table 1.

The first eight columns in Table 1 show the basic features of 47 neutron monitors. Figure 4 shows the geographical distribution of these stations, and Figure 5 shows their longitudinal distribution in terms of 15-degree bins of local time. As discussed in Su, Yu, and Yong *et al.* (2008), if the start times of the main phase (indicated by T_2 in Figure 3) in Fd
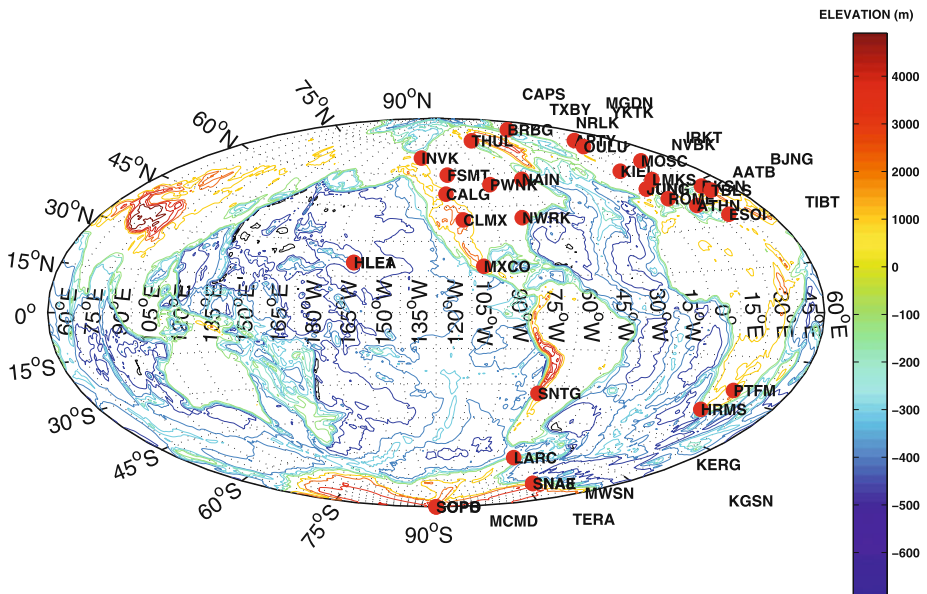
Figure 4 The geographic distribution of 47 ground-based stations which registered a counting rate drop from 1 to 28 November 2004. A Hammer–Aitoff projection, which is an equal-area projection with curved meridians and parallels, is applied. Red circles denote the geographic locations of neutron monitors used, and the contours approximately represent the elevation values of the Earth (the scale is shown in the right-hand corner of Figure 4).

Table 1 Summary of the obtained results from hourly cosmic ray intensities registered by 47 ground-based neutron monitors for the investigated event with amplitude $>4\%$ during the studied interval.

No.	Name	Long (°)	Lat (°)	Alt (m)	R_c	Type	LT	T_1 mm/dd/hh	T_2 mm/dd/hh	T_3 mm/dd/hh	T_4 mm/dd/hh	ΔT_{21} (h)	ΔT_{32} (h)	ΔT_{43} (h)
1	AATB	76.92	43.25	3340	6.61	18NM64	UT+05h	11/01/10	11/07/19	11/10/04	11/17/06	153	57	170
2	APTY	33.33	67.55	177	0.57	18NM64	UT+02h	11/02/17	11/07/19	11/10/04	11/18/12	122	57	179
3	ATHN	23.78	37.98	260	8.53	6NM64	UT+02h	11/05/12	11/07/19	11/10/05	11/14/16	55	58	107
4	BJNG	116.26	39.08	48	10.0	18NM64	UT+08h	11/02/02	11/07/19	11/10/02	11/14/06	137	55	100
5	BKSN	42.69	43.28	1700	5.6	6NM64	UT+03h	10/31/09	11/07/19	11/10/06	11/15/14	178	59	128
6	BRBG	14.22	78.06	51	0.0	18NM64	UT+01h	11/02/13	11/07/19	11/10/04	11/18/12	126	57	200
7	CALG	−114.13	51.08	1128	1.08	12NM64	UT−08h	11/02/21	11/07/19	11/10/02	11/16/22	118	55	164
8	CAPS	180	68.55	0.0	0.45	12NM64	UT+12h	11/03/05	11/07/19	11/10/03	11/18/02	110	56	191
9	CLMX	−106.18	39.37	3400	2.99	12IGY	UT−07h	11/02/19	11/07/17	11/10/04	11/17/22	117	59	186
10	ESOI	35.8	33.3	2025	10.8	6NM64	UT+02h	10/31/11	11/07/19	11/10/04	11/14/07	176	57	99
11	FSMT	−112.0	60.0	0.0	0.0	18NM64	UT−07h	11/02/23	11/07/19	11/10/02	11/18/21	116	55	211
12	HLE1	−156.25	20.72	3030	12.91	12IGY	UT−10h	11/02/19	11/07/19	11/10/04	11/13/19	120	57	87
13	HLEA	−156.27	20.72	3052	12.91	12IGY	UT−10h	11/02/21	11/07/19	11/10/05	11/13/20	118	58	88
14	HRMS	19.23	−34.42	26	4.58	12NM64	UT+01h	11/02/14	11/07/19	11/10/04	11/16/14	125	57	154
15	INVK	−133.72	68.35	21	0.17	18NM64	UT−09h	11/02/23	11/07/19	11/10/02	11/18/03	116	55	193
16	IRKT	104.03	52.47	435	3.64	18NM64	UT+07h	11/03/09	11/07/19	11/10/03	11/15/11	106	56	128
17	JUN1	7.98	46.55	3570	4.54	18IGY	UT+0h	11/03/14	11/07/19	11/10/04	11/16/11	173	57	151
18	JUNG	7.98	46.55	3475	4.54	3NM64	UT+0h	10/31/15	11/07/19	11/10/04	11/19/20	172	57	232
19	KERG	70.27	−49.35	33	1.14	18NM64	UT+05h	10/31/20	11/07/19	11/10/20	11/17/11	167	73	159
20	KGSN	147.29	−42.99	65	1.81	18NM64	UT+10h	11/03/02	11/07/19	11/10/02	11/18/01	113	55	191
21	KIEL	10.1	54.3	54	2.36	18NM64	UT+01h	11/02/16	11/07/17	11/10/04	11/16/14	121	59	154
22	LARC	−58.96	−62.2	40	3.0	6NM64	UT−04h	10/31/16	11/07/19	11/10/04	11/16/18	171	57	158
23	LMKS	20.22	49.2	2634	3.98	12NM64	UT+01h	10/31/15	11/07/19	11/10/04	11/28/12	172	57	440
24	MCMD	166.6	−77.9	48	0.0	18NM64	UT+11h	11/02/21	11/07/19	11/10/01	11/17/23	118	54	190

Table 1 (*Continued*)

No.	Name	Long (°)	Lat (°)	Alt (m)	R_c	Type	LT	T_1 mm/dd/hh	T_2 mm/dd/hh	T_3 mm/dd/hh	T_4 mm/dd/hh	ΔT_{21} (h)	ΔT_{32} (h)	ΔT_{43} (h)
25	MGDN	151.05	60.04	220	2.09	18NM64	UT+10h	11/03/09	11/07/19	11/10/09	11/18/07	106	62	190
26	MOSC	37.32	55.47	200	2.43	24NM64	UT+02h	11/02/14	11/07/19	11/10/04	11/16/09	125	57	149
27	MWSN	62.88	−67.6	0	0.22	18NM64	UT+04h	11/01/21	11/07/13	11/10/04	11/17/14	142	63	178
28	MXCO	−99.2	19.33	2274	9.53	6NM64	UT−07h	11/02/19	11/07/21	11/10/04	11/15/14	122	55	130
29	NAIN	−61.7	56.6	0	0.0	18NM64	UT−04h	11/02/21	11/07/19	11/10/04	11/16/20	118	57	160
30	NRLK	88.05	69.26	0	0.58	18NM64	UT+06h	10/31/09	11/07/19	11/10/09	11/17/10	178	62	169
31	NVBK	83.0	54.48	163	2.87	24NM64	UT+06h	11/02/09	11/07/19	11/09/23	11/17/06	130	52	175
32	NWRK	−75.7	39.7	50	2.09	9NM64	UT−05h	11/02/20	11/07/19	11/10/01	11/16/23	119	54	166
33	OULU	25.47	65.06	0	0.78	9NM64	UT+02h	11/02/12	11/07/19	11/10/04	11/17/14	127	57	178
34	PTFM	27.1	−26.68	1351	7.0	15IGY	UT+02h	11/03/13	11/07/17	11/10/20	11/16/08	100	75	132
35	PWNK	−85.0	55.0	0	0.0	18NM64	UT−06h	11/02/12	11/07/19	11/10/02	11/17/23	118	55	189
36	ROME	12.52	41.9	60	6.32	17NM64	UT+01h	11/02/14	11/07/19	11/10/04	11/15/12	125	57	128
37	SNA8	−2.85	−71.67	856	0.91	4NM80	UT−0h	11/02/13	11/07/21	11/10/04	11/17/21	128	55	185
38	SNAE	−2.85	−71.67	856	0.86	6NM64	UT−0h	11/02/20	11/07/21	11/10/01	11/18/16	121	52	207
39	SNTG	−70.71	−33.48	570	11.0	6NM64	UT−05h	11/02/15	11/07/17	11/10/04	11/13/17	122	59	85
40	SOPB	0.0	−90.0	2820	0.09	6NM64	UT+0h	11/02/20	11/07/19	11/10/01	11/19/13	119	54	228
41	SOPO	0.0	−90.0	2820	0.09	3NM64	UT+0h	11/02/20	11/07/19	11/10/01	11/19/14	119	54	229
42	TBLS	44.48	41.43	510	6.73	18NM64	UT+03h	11/03/09	11/07/19	11/10/04	11/15/12	106	57	128
43	TERA	140.02	−66.67	45	0.02	9NM64	UT+09h	11/02/16	11/07/19	11/10/01	11/17/12	123	54	179
44	THUL	−68.8	76.6	260	0.0	9NM64	UT−05h	11/02/22	11/07/19	11/10/05	11/18/10	117	58	197
45	TIBT	90.53	30.11	4300	14.1	28NM64	UT+06h	11/02/23	11/07/19	11/10/05	11/11/07	115	58	26
46	TXBY	128.54	71.36	0	0.48	18NM64	UT+09h	11/02/22	11/07/19	11/10/16	11/17/14	117	69	166
47	YKTK	129.43	62.01	105	1.65	18NM64	UT+09h	11/03/06	11/07/19	11/10/14	11/22/06	109	67	280

The first eight columns show, respectively, the station number, station name (expressed by four letters taken from Asipenka *et al.*, 2009), the longitude, latitude, and altitude (Alt) of the station, nominal geomagnetic cut-off rigidity (R_C), the type of neutron monitor, and the local time (LT) of each station. The next four columns indicate the onset time of the initial phase (T_1), the end time of the initial phase (*i.e.* the onset time of the main phase, T_2), the end time of the main phase (*i.e.* the onset time of the recovery phase, T_3), and the end time of the recovery phase (T_4), respectively. The last three columns show the durations of the initial phase (ΔT_{21}), main phase (ΔT_{32}), and recovery phase (ΔT_{43}), respectively.
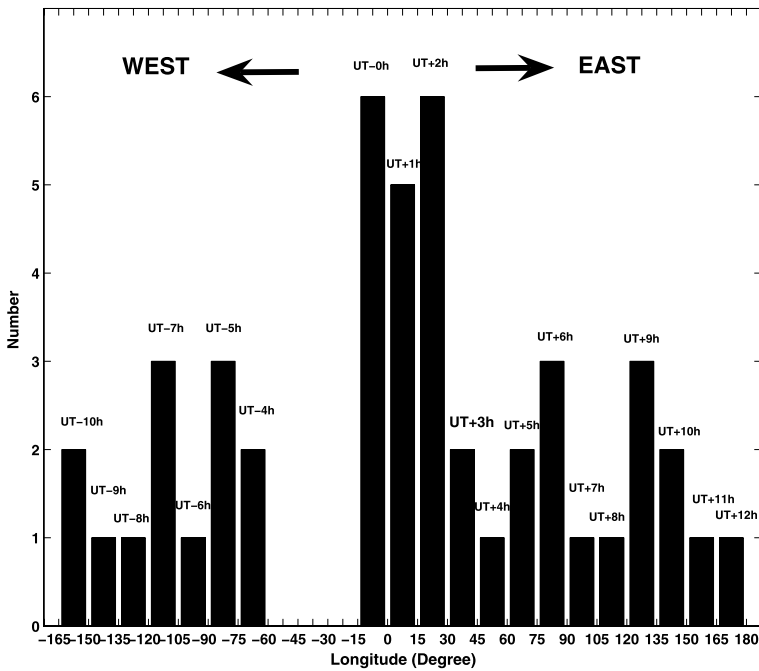
Figure 5 Longitudinal distribution of 47 ground-based neutron monitors in terms of 15-degree bins of local time.

events deduced from different stations cluster around an identical time, we define it as a simultaneous event. Inspection of the values of T_2 in Table 1 shows that a large fraction (39/47) of the start times of the main phase (the earliest catastrophe point in CR variation indicated by T_2 in Figure 3) was clustered at 19:00 UT on 7 November, independent of the location of the station. The dispersion in the onset times is 2 to 3 hours among different stations, and only a small fraction (1/47) is outside the data window from 17:00 to 21:00 UT on 7 November. Moreover, a large fraction (about 45%) of the onset times of the recovery phase of the Fd was clustered at 04:00 UT on 10 November, regardless of the location of the station. The dispersion in the onset times is also 2 to 3 hours among different stations, and therefore only a small fraction (7/47) is outside the data window from 01:00 to 06:00 UT on 10 November. Both of them consistently indicate that the Fd event studied, which was caused by strong disturbances in the interplanetary medium, was globally simultaneous. Our analysis suggests that the earliest catastrophe point in CR variation preceded the arrival time of the first cloud by about 3 hours. It is consistent with the finding that the CR decrease starts earlier than the arrival of the cloud, because it is preceded by a shock (Badruddin, Yadav, and Yadav, 1986). Considering the results shown in Figures 1 and 2, the time of minimum intensity (04:00 UT, 10 November) lagged behind the arrival time of the first cloud (cloud one in Figures 1 and 2) by about 2.3 days, because the superposed influence from the second magnetic cloud (cloud two in Figures 1 and 2) starting at 17:00 UT on 8 November 2004 (Harra *et al.*, 2007) enhanced the amplitudes of the Fds. The superposition of counting rates from multiple stations shows that the Fds started nearly at the arrival of the third shock.

We divide the latitude distribution of 47 stations into four groups, and hence they are $S90° - S60°$, $S60° - S30°$, $N30° - N60°$ and $N60° - N90°$, respectively. The corresponding mean values of percentage variation which fall into the above four groups turned out to

be -13.8%, -10.0%, -9.8%, and -11.9%, respectively. The average amplitudes of Fds observed in the southern hemisphere are larger. Therefore, we may conclude that the disturbance was asymmetric when it reached the Earth, inclined to the southern hemisphere. The CMEs which caused the geomagnetic storms should have moved to the magnetopause southward and interacted with the magnetosphere continuously. This property is confirmed by investigating the CR variation observed at sub-polar stations (*i.e.* SOPB and BRBG in Figure 2).

By looking at the intensity profiles, we can find both two-step and quasi-three-step Fds. The detailed data of two-step Fds listed in Table 2 show that the first step corresponds to the sheath region and the second one to the passage of the magnetic cloud.

By using different models for the geomagnetic field (*i.e.* Ts89, Ts03), many previous authors (Belov *et al.*, 2005; Kudela, Bucik, and Bobik, 2008; Tyasto *et al.*, 2009) calculated the cutoff rigidity at low-latitude stations and mid-latitude ones during the strong magnetic storm in November 2004, both theoretically and experimentally. A strong decrease in cosmic-ray rigidity was found, in spite of the fact that the dependences of the first-step amplitude, the second-step amplitude, and the duration of the recovery time in the Fd event on the nominal geomagnetic cut-off rigidity (R_c) present a simple linear relation in our statistical analyses. Future efforts in this direction should be focused on the computations utilizing the data from all 47 stations involved, by applying different models, with the goal to describe the time variations of the cosmic-ray cutoff rigidity.

4. Summary and Conclusions

In spite of the fact that the influence of magnetic clouds on the variations of cosmic rays from different neutron-monitor stations is complex and varies significantly from case to case, we can still draw the following conclusions.

i) By using the wavelet decomposition, the catastrophe points in the counting rate of cosmic rays are identified, and the earliest one of several catastrophe points seen in the wavelet decomposition in the selected time window is defined as the onset time of the main phase in a Fd event. Hence, clearer definitions of the initial phase, main phase, and recovery phase are proposed.

ii) The onset time of the main phase preceded the arrival time of the first cloud by about 3 hours and a large fraction of them (39/47) was found to originate from the sheath region as indicated by large fluctuations in magnetic field vectors at 19:00 UT on 7 November 2004, regardless of the station location. It is consistent with the conclusion that the CR decrease starts earlier than the arrival of the cloud and is due to the shock in front of the cloud.

iii) About 45% of the onset times of the recovery phase of the Fds was clustered at 04:00 UT on 10 November, independent on the station position. Comparison with time variations from different neutron monitors reveals the global simultaneity of this Fd event.

iv) The interplanetary disturbance was asymmetric when it reached the Earth, being inclined to the southern hemisphere. The CMEs which caused the geomagnetic storms should have moved to the magnetopause southward and interacted with the magnetosphere continuously.

v) Our analysis in this paper has clearly demonstrated that the sheath region between the shock and the magnetic cloud, particularly the enhanced turbulent magnetic field, results in the scattering of cosmic-ray particles, and causes the following Fds. Maybe it is the

Table 2 List of the characteristics of two-step Forbush decreases deduced from different neutron-monitor stations.

No.	NM station	T_2 dd/hh	T_A dd/hh	T_3 dd/hh	tt$_1$ (h)	tt$_2$ (h)	First step amplitude (%)	Second step amplitude (%)
1	AATB	07/19	07/23	10/04	4	53	−6.7	−8.9
2	APTY	07/19	07/24	10/04	5	52	−7.3	−11.9
3	ATHN	07/19	07/23	10/05	4	54	−4.2	−5.9
4	BJNG	07/19	07/21	10/02	2	53	−3.2	−6.8
5	BKSN	07/19	07/23	10/06	4	55	−5.5	−8.1
6	BRBG	07/19	08/13	10/04	18	39	−8.6	−13.5
7	CALG	07/19	08/15	10/02	20	35	−8.9	−13.0
8	CAPS	07/19	08/15	10/03	20	36	−7.4	−11.8
9	CLMX	07/17	08/15	10/04	22	37	−9.9	−13.3
10	ESOI	07/19	07/23	10/04	4	53	−4.2	−6.2
11	FSMT	07/19	08/15	10/02	20	35	−8.5	−12.9
12	HLE1	07/19	08/16	10/04	21	36	−2.9	−6.9
13	HLEA	07/19	08/15	10/05	20	38	−3.0	−6.4
14	HRMS	07/19	07/23	10/04	4	53	−5.4	−8.9
15	INVK	07/19	07/14	10/02	19	36	−7.3	−11.4
16	IRKT	07/19	07/23	10/03	4	52	−5.0	−9.4
17	JUN1	07/19	07/23	10/04	4	53	−6.0	−9.8
18	JUNG	07/19	08/17	10/04	22	35	−6.8	−10.5
19	KERG	07/19	08/16	10/20	21	52	−10.0	−12.1
20	KGSN	07/19	07/23	10/02	4	51	−6.6	−11.3
21	KIEL	07/17	08/16	10/04	23	36	−6.8	−11.0
22	LARC	07/19	08/04	10/04	9	48	−7.1	−12.1
23	LMKS	07/19	08/17	10/04	22	35	−9.2	−13.3
24	MCMD	07/19	08/04	10/01	9	45	−8.7	−12.6
25	MGDN	07/19	07/23	10/09	4	58	−6.8	−11.7
26	MOSC	07/19	08/17	10/04	22	35	−7.4	−10.3
27	MWSN	07/13	08/17	10/04	28	35	−9.4	−12.1
28	MXCO	07/21	08/03	10/04	6	49	−4.8	−8.7
29	NAIN	07/19	08/04	10/04	9	48	−8.2	−12.4
30	NRLK	07/19	08/15	10/09	20	42	−8.0	−10.5
31	NVBK	07/19	08/17	09/23	22	30	−7.0	−9.9
32	NWRK	07/19	08/03	10/01	8	46	−7.7	−11.7
33	OULU	07/19	08/01	10/04	6	51	−7.7	−12.5
34	PTFM	07/17	08/15	10/20	22	53	−3.9	−7.7
35	PWNK	07/19	08/14	10/02	19	36	−9.8	−13.0
36	ROME	07/19	07/23	10/04	4	53	−3.7	−7.3
37	SNA8	07/21	07/25	10/04	4	51	−10.4	−14.2
38	SNAE	07/21	07/27	10/01	6	46	−9.0	−13.3
39	SNTG	07/17	09/01	10/04	32	27	−3.3	−7.8
40	SOPB	07/19	08/16	10/01	21	33	−13.9	−17.4
41	SOPO	07/19	08/16	10/01	21	33	−12.4	−15.9

Table 2 (*Continued.*)

No.	NM station	T_2 dd/hh	T_A dd/hh	T_3 dd/hh	tt$_1$ (h)	tt$_2$ (h)	First-step amplitude (%)	Second-step amplitude (%)
42	TBLS	07/19	07/23	10/04	4	53	−6.9	−8.4
43	TERA	07/19	08/04	10/01	9	45	−7.4	−12.9
44	THUL	07/19	08/04	10/05	9	49	−7.4	−12.7
45	TIBT	07/19	07/21	10/05	2	56	−2.6	−4.4
46	TXBY	07/19	08/15	10/16	20	49	−7.7	−11.4
47	YKTK	07/19	07/23	10/14	4	63	−8.7	−12.0

The columns represent the station number, station name, the end time of the initial phase (*i.e.* the onset time of main phase, T_2), T_A, the end time of the main phase (*i.e.* the onset time of the recovery phase, T_3), the duration of the first step (tt$_1$), the duration of the second step (tt$_2$), and the amplitudes of the two-step Fds, respectively.

most effective mechanism to produce a transient depression in cosmic-ray variations. This conclusion is in accordance with the hypothesis made by Badruddin, Venkatesan, and Zhu (1991).

The results mentioned above provide several observational constraints for more detailed simulations of the Forbush decrease events with time-dependent cosmic-ray modulation models.

References

Afraimovich, E.L., Voeykov, S.V., Perevalova, N.P., Ratovsky, K.G.: 2006, *Geomagn. Aeron.* **46**, 603.

Alania, M.V., Wawrzynczak, A.: 2008, *Astrophys. Space Sci. Trans.* **4**, 59.

Ananth, A.G., Venkatesan, D.: 1993, *Solar Phys.* **143**, 373.

Asipenka, A.S., Belov, A.V., Eroshenko, E.A., Klepach, E.G., Oleneva, V.A., Yanke, V.G.: 2009, *Adv. Space Res.* **43**, 708.

Badruddin, O.: 2000, *Nuovo Cim. C* **23**, 217.

Badruddin, O.: 2002, *Solar Phys.* **209**, 195.

Badruddin, O.: 2006, *J. Astrophys. Astron.* **27**, 209.

Badruddin, O., Yadav, R.S., Yadav, N.R.: 1986, *Solar Phys.* **105**, 413.

Badruddin, O., Venkatesan, D., Zhu, B.Y.: 1991, *Solar Phys.* **134**, 203.

Barnden, L.R.: 1973, *Proc. 13th Int. Cosm. Ray Conf.* **2**, 1277.

Belov, A.V., Bieber, J.W., Eroshenko, E.A., Evenson, P., Pyle, R., Yanke, V.G.: 2003, *Adv. Space Res.* **31**, 919.

Belov, A.V., Baisultanova, L., Buetikofer, R., Eroshenko, E., Flueckiger, E.O., Mariatos, H., Mavromichalaki, H., Pchelkin, V., Yanke, V.G.: 2005, *Proc. 29th Int. Cosm. Ray Conf.* **2**, 385.

Belov, A.V., Gushchina, R.T., Eroshenko, E.A., Yudakhin, K.F., Yanke, V.G.: 2007, *Geomagn. Aeron.* **47**, 251.

Bisi, M.M., Jackson, B.V., Hick, P.P., Buffington, A., Odstrcil, D., Clover, J.M.: 2008 *J. Geophys. Res.* **113**, A00A11.

Burlaga, L.F., Sittler, E., Mariani, F., Schwenn, R.: 1981, *J. Geophys. Res.* **86**, 6673.

Cane, H.V.: 2000a, *Space Sci. Rev.* **93**, 55.

Cane, H.V., Richardson, I.G.: 1995, *J. Geophys. Res.* **100**, 1755.

Cane, H.V., Richardson, I.G., St Cyr, O.C.: 2000b, *Geophys. Res. Lett.* **27**, 3591.

Cheng, A.F., Sarris, E.T., Dodopoulos, C.: 1990, *Astrophys. J.* **350**, 413.

Culhane, J.L., Pohjolainen, S., van Driel-Gesztelyi, L., Manoharan, P.K., Elliott, H.A.: 2007, *Adv. Space Res.* **40**, 1807.

Dasso, S., Mandrini, C.H., Demoulin, P., Luoni, M.L.: 2006, *Astron. Astrophys.* **455**, 349.

Dasso, S., Nakwacki, M.S., Demoulin, P., Mandrini, C.H.: 2007, *Solar Phys.* **244**, 115.

Dorman, L.I.: 2004, *Cosmic Rays in the Earth's Atmosphere and Underground*, Kluwer Academic, Dordrecht. Sections 18.12 and 18.14.

Dorman, L.I.: 2005, *Ann. Geophys.* **23**, 2997.

Dorman, L.I., Iucci, N., Villoresi, G.: 1995, *Proc. 24th Int. Cosm. Ray Conf.* **4**, 892.

Dorotovic, I., Kudela, K., Lorenc, M., Rybansky, M.: 2008, *Solar Phys.* **250**, 339.

Eroshenko, E., Belov, A., Mavromichalaki, H., Mariatos, G., Oleneva, V., Plainaki, C., Yanke, V.: 2004, *Solar Phys.* **224**, 345.

Gonzalez, W.D., Joselyn, J.A., Kamide, Y., Kroehl, H.W., Rostoker, G., Tsurutani, B.T., Vasyliunas, V.M.: 1994, *J. Geophys. Res.* **99**, 5771.

Gopalswamy, N., Yashiro, S., Akiyama, N.: 2007, *J. Geophys. Res.* **112**, A06112.

Gopalswamy, N., Lara, A., Yashiro, S., Kaiser, M.L., Howard, R.A.: 2001, *J. Geophys. Res.* **106**, 29207.

Gopalswamy, N., Akiyama, S., Yashiro, S., Michalek, G., Lepping, R.P.: 2008, *J. Atmos. Solar-Terr. Phys.* **70**, 245.

Grigorenko, E.I., Lysenko, V.N., Pazyura, S.A., Taran, V.I., Chernogor, L.F.: 2007, *Geomagn. Aeron.* **47**, 720.

Harra, L.K., Crooker, N.U., Mandrini, C.H., van Driel-Gesztelyi, L., Dasso, S., Wang, J.X., Elliott, H., Attrill, G., Jackson, B.V., Bisi, M.M.: 2007, *Solar Phys.* **244**, 95.

Ifedili, S.O.: 2006, *Earth Planets Space* **58**, 659.

Jamsen, T., Usoskin, I.G., Raiha, T., Sarkamo, J., Kovaltsov, G.A.: 2007, *Adv. Space Res.* **40**, 342.

Kane, R.P.: 2006, *Solar Phys.* **234**, 353.

Kudela, K., Brenkus, R.: 2004, *J. Atmos. Solar-Terr. Phys.* **66**, 1121.

Kudela, K., Bucik, R., Bobik, P.: 2008, *Adv. Space Res.* **42**, 1300.

Le Roux, J.A., Potgieter, M.S.: 1991, *Astron. Astrophys.* **243**, 531.

Longcope, D., Beveridge, C., Qiu, J., Ravindra, B., Barnes, G., Dasso, S.: 2007, *Solar Phys.* **244**, 45.

Marcz, F.: 1992, *Planet. Space Sci.* **40**, 979.

Mavromichalaki, H., Souvatzoglou, G., Sarlanis, C., Mariatos, G., Plainaki, C., Gerontidou, M., Belov, A., Eroshenko, E., Yanke, V.: 2006, *Adv. Space Res.* **37**, 1141.

Mulder, M.S., Moraal, H.: 1986, *Astrophys. J.* **303**, L75.

Nakwacki, M.S., Dasso, S., Demoulin, P., Mandrini, C.H.: 2008, *Geofis. Int.* **47**, 295.

Panasenko, S.V., Chernogor, L.F.: 2007, *Geomagn. Aeron.* **47**, 608.

Pirog, O.M., Polekh, N.M., Voeykov, S.V., Zherebtsov, G.A., Tatarinov, P.V.: 2007, *Adv. Space Res.* **39**, 1335.

Pohjolainen, S., van Driel-Gesztelyi, L., Culhane, J.L., Manoharan, P.K., Elliott, H.A.: 2007, *Solar Phys.* **244**, 167.

Pulkkinen, T.I., Partamies, N., Huttunen, K.E.J., Reeves, G.D., Koskinen, H.E.J.: 2007, *Geophys. Res. Lett.* **34**, L02105.

Qiu, J., Hu, Q., Howard, T.A., Yurchyshyn, V.B.: 2007, *Astrophys. J.* **659**, 758.

Rana, D.S., Sharma, N.K., Yadav, R.S.: 1996, *Solar Phys.* **167**, 371.

Su, Y.O., Yu, Y., Yong, H.K.: 2008, *J. Geophys. Res.* **113**, A01103.

Tyasto, M.I., Danilova, O.A., Dvornikov, V.M., Sdobnov, V.E.: 2009, *Bull. Russ. Acad. Sci. Phys.* **73**, 367.

Usoskin, I.G., Braun, I., Gladysheva, O.G., Horandel, J.R., Jamsen, T., Kovaltsov, G.A., Starodubtsev, S.A.: 2008, *J. Geophys. Res.* **113**, A07102.

Venkatesan, D., Badruddin, O., Ananth, A.G., Pillai, S.: 1992, *Solar Phys.* **137**, 345.

Wang, Y., Zheng, H., Wang, S., Ye, P.: 2005, *Astron. Astrophys.* **434**, 309.

Wang, J.X., Zhang, Y.Z., Zhou, G.P., Harra, L.K., Williams, D.R., Jiang, Y.C.: 2007, *Solar Phys.* **244**, 75.

Yermolaev, Yu.I., Zelenyi, L.M., Zastenker, G.N., Petrukovich, A.A., Yermolaev, M.Yu., Nikolaeva, N.S., *et al.*: 2005, *Geomagn. Aeron.* **45**, 681.

Zhang, G., Burlaga, L.F.: 1988, *J. Geophys. Res.* **93**, 2511.